Unsupervised Discrepancy-Based Domain Adaptation Network to Detect Rail Joint Condition

Gao-Feng Jiang, Su-Mei Wang, *Member, IEEE*, Yi-Qing Ni, *Member, IEEE*, and Wen-Qiang Liu, *Member, IEEE*

***Abstract*— Damage to maglev rail joints, which connect adjacent rail segments, threatens the safety and comfort of railway systems. Machine learning methods have been used in combination with online monitoring data to assess the health conditions of maglev rail joints. However, most of the existing methods rely on the data collected in controlled scenarios, such as those involving constant train operation speeds. Given the diversity of operational conditions, a model learned from one known case (source domain) cannot be directly applied to the case of interest (target domain). Therefore, this article proposes a domain adaptation (DA) approach to diagnose the health conditions of maglev rail joints in complex operational conditions. The DA is unsupervised because the source and target domains are characterized by labeled and unlabeled samples, respectively. DA is implemented by integrating the sample moments with different orders into the transfer loss of a neural network. By minimizing the transfer loss, the domain shift caused by the difference in the operational conditions can be reduced, and the knowledge of features learned from the neural network is transferred from the source domain to the target domain. The proposed approach is validated over a dataset of time–frequency spectrograms (TFSs) derived from the experimental acceleration data of maglev rail joints in two operation modes: stable passing and braking. The proposed approach can successfully identify the conditions of the maglev rail joints, i.e., bolt-looseness-caused rail step, misalignment-caused lateral dislocation, and normal condition, even when the operation mode of the maglev train changes.**

***Index Terms*— Maglev rail joints, structural damage detection, transfer learning (TL), unsupervised domain adaptation (DA).**

I. Introduction

MAGLEV is a kind of noncontact transportation system with the advantage of less noise and friction. In such systems, suspension and guidance are realized through the electromagnetic force provided by U-shaped magnets and F-type rails [1]. The fluctuation between electromagnet and F-type rails should be confined within 2–3 mm to ensure the stability of maglev trains, and such a small fluctuation invokes a high requirement for the condition of F-type rail. However, the F-type rail is prone to deformation due to temperature changes, foundation settlements, and force actions. Temperature changes play the most influential role among those causes. The growing temperature difference of the maglev guideway will lead to a great temperature gradient and cause a significant increase in deformation. Hence, a seam, known as the rail joint, is considered in the design to allow for the deformation. Maglev rail joints are typically used to connect F-type rails to satisfy the control requirement of the suspension gap between the electromagnet and rail and enable slight movement between two adjacent F-type rails due to temperature-induced expansion and contraction [2], [3]. Notably, maglev rail joints are prone to structural damage because of environmental changes, train excitation, and installation errors [4]. This structural damage typically manifests as bolt-looseness-caused rail step and misalignment-caused dislocation, which may lead to rail irregularity and decreased electromagnetic force, respectively [2], [5]. According to the experimental results on several current maglev lines, the rail step and lateral dislocation often occur at maglev rail joints in practice. Such damage scenarios may lead to rough suspension gap fluctuations, suspension control failure, and even a sudden clash between the electromagnet and the rail. Large impacts on the rail are generated by repeated suspension gap fluctuations [6], causing maglev rail joints to become the weakest part of the maglev rail and reducing the ride comfort of maglev trains [7]. Moreover, the large impacts and dynamic suspension forces acting on the maglev rail joints aggravate structural deterioration [6], [8]; thus, bolts get loose, rail ends become battered, and cracks develop in the F-type rail.

To avoid such scenarios, the condition of maglev rail joints is typically visually inspected. Such manual observations may be unreliable, intrusive, and unsafe [8]. Therefore, to maintain the safe operation of maglev systems, intelligent techniques for rail joint monitoring must be developed. The successful practices of intelligent rail joint monitoring have been witnessed. For example, the axle box acceleration data measured from the rail vehicle are used to monitor the conditions of rail joints [8], [9]. In [8] and [9], the wavelet transform algorithm is employed to extract the characteristics of rail joint damage

Manuscript received 18 July 2023; accepted 23 August 2023. Date of publication 18 September 2023; date of current version 9 October 2023. This work was supported in part by the National Natural Science Foundation of China under Grant U1934209; in part by the Wuyi University's Hong Kong and Macao Joint Research and Development Fund under Grant 2019WGALH15, Grant 2019WGALH17, and Grant 2021WGALH15; in part by the Innovation and Technology Commission of Hong Kong SAR Government, China, under Grant K-BBY1; and in part by the Hong Kong Polytechnic University (PolyU) Startup Fund for Research Assistant Professors (RAPs) through the Strategic Hiring Scheme under Grant P0039260. The Associate Editor coordinating the review process was Dr. Ke Feng. *(Corresponding author: Su-Mei Wang.)*

The authors are with the Department of Civil and Environmental Engineering, The Hong Kong Polytechnic University, Hong Kong, China, and also with the National Rail Transit Electrification and Automation Engineering Technology Research Center (Hong Kong Branch), Hong Kong, China (e-mail: gao-feng.jiang@connect.polyu.hk; may.sm.wang@polyu.edu.hk; ceyqni@polyu.edu.hk; wqiang.liu@polyu.edu.hk).

Digital Object Identifier 10.1109/TIM.2023.3316221

for rail joint monitoring. Chang et al. [10] measured the dynamic response of rail to identify the misalignment-caused damage at rail joints. The abovementioned studies have proposed effective methods to thoroughly investigate the damage mechanisms and recognize rail joint damage. However, the damage detection methods in [8], [9], and [10] are realized through the track inspection wagon, which still relies on labor to collect massive data. Besides, these methods require manual feature extraction from data for damage detection. Thus, there is still room for developing convenient and cost-effective rail joint damage detection and classification methods.

Deep learning (DL) algorithms can be applied for the damage detection of rail joints as they can automatically extract discriminative features from a massive amount of data. Among DL algorithms, convolutional neural networks (CNNs) are an effective feature extractor. Surface defect detection based on CNNs is a popular topic. Different surface defects can be classified through camera images [11], [12]. However, the damage to a rail joint is not always visible. Vibration-based CNNs become an alternative by extracting features from numerous raw vibration signals [13]. In the field of structural health monitoring, CNN and vibration signals have been used to inspect structural damage [14], [15], [16], [17], [18]. For example, a CNN model trained with time-series data of bridge acceleration responses from a set of shake table tests was used to identify and quantify four types of concrete bridge damage [16]. In addition to directly using the data in the time domain, the implicit information in the frequency domain can be used for structural damage detection. Duan et al. [17] trained a CNN model by using the Fourier amplitude spectra of acceleration responses to detect the damage of a tied-arch bridge. Using a CNN model built with the time–frequency spectrogram (TFS) of acceleration responses, Wang et al. [18] detected multiple damages to maglev rail joints. Notably, in these studies, the training and testing data are independent and identically distributed (i.i.d). In other words, the existing approaches ignore discrepancies in the distribution and have been validated for only a given data distribution. In the real world, the training data are often acquired from specific cases, whereas the testing data might be collected considering various operational and environmental conditions. Consequently, the i.i.d hypothesis fails, creating the domain shift between the training and testing data [19]. This problem can be overcome by collecting new labeled data and building an updated model. However, these processes are time-consuming and impractical for most industrial scenarios [20].

Recently, transfer learning (TL) has emerged as a promising approach to solving the domain shift issue. TL can help enhance the model performance by allowing the model to learn the knowledge from previous tasks and apply this knowledge to new and similar tasks. As a type of TL, domain adaptation (DA) realizes knowledge transfer by reweighting the samples in model training or identifying a shared space to match the inconsistent data distribution [21]. In recent years, DA has been widely applied for structural damage detection, such as the damage of multistory buildings, with the source and target domains corresponding to numerical and experimental data, respectively [20], [22]. In addition, many researchers have used DA for damage detection considering changes in the operational state of structural components, such as in the fault diagnosis of rolling bearings [23] and power plant thermal systems [24]. In railway engineering, DA has been used for the damage detection of rail vehicles. Yu et al. [25] used conditional adversarial DA to predict the faults of a gearbox and shaft at different running speeds. Qin et al. [26] developed a stepwise adaptive CNN to classify the faults of a high-speed train bogie with a continuously varying vehicle speed. Chen et al. [27] established a semisupervised adversarial DA to assess the condition of high-speed train wheels under different surrounding environments.

In practice, there are also different working conditions in maglev lines. Variations in the maglev train speeds and running status (e.g., stable passing, suspension, and braking) affect the structural response of maglev rail joints. Consequently, a large domain shift [29] exists in the vibration signals collected from one maglev rail joint under different operation modes. The performance of a model trained by data from one operation mode may deteriorate when it is applied to another mode due to the change in the external excitation in different modes. Thus, the above evidence motivates us to use DA for maglev rail joint damage detection. However, regarding rail joint damage detection, only a few novel studies used DL algorithms [18], [28], and even none of the studies used TL algorithms, e.g., DA algorithms. This may be because the common research objects using DA for damage detection are structural components such as bearings and gears. The cross-domain features of bearing and gear damage usually appear continuously at certain frequencies, while the cross-domain features of rail joint damage are hard to capture since they appear shortly and usually at nonfixed and high frequencies. In this study, an unsupervised discrepancy-based DA network (UDDAN) is proposed to detect the maglev rail joint damage condition considering the actual operation modes. The data, i.e., vibration signals from maglev rail joints, are often collected with a high frequency, which makes the data numerous. Meanwhile, the data for damaged cases are much fewer than for normal cases. In addition, the labeling is time-consuming and requires appropriate observations, especially for the damaged data. Unlike supervised algorithms, unsupervised algorithms eliminate the need for labeling. Therefore, the UDDAN is proposed to classify the maglev rail joint condition even if the labels are unavailable.

The UDDAN implements the following steps. First, the acceleration responses of two types of damaged maglev rail joints and an undamaged maglev rail joint are collected from a monitoring system installed on the maglev test line in Shanghai, China. The acceleration responses are processed to samples reflecting the time–frequency features of maglev rail joints in two operation modes (stable passing and braking). Subsequently, a series of samples are input to the UDDAN model, which derives domain-invariant time–frequency features of maglev rail joints in two operation modes. The adaptation layer is placed at the top of the model to ensure that the data distribution of one mode (source domain) is

like that of the other mode (target domain) to minimize the domain discrepancy caused by the operation mode. The classification layer allows the model to detect the condition of maglev rail joints in both modes after sufficient alignment of the data distribution. Compared to those existing DA algorithms developed and verified through benchmark datasets covering a wide range of categories, e.g., Office-31 and Office-Home, UDDAN is trained from the dataset of TFSs. This dataset is much smaller in variety and has less cross-category difference than benchmark datasets. Therefore, the existing algorithms may fail to extract discriminative features between TFSs. In contrast, UDDAN enables feature extraction in a different way to those existing algorithms. Hence, UDDAN is tailored for the maglev rail damage detection problem.

The key contributions of this research can be summarized as follows.

1) To the best of the authors' knowledge, this study represents the first attempt at DA-based maglev rail joint damage detection and highlights the key role of DA in improving the classification performance. Maglev rail joint damage detection is affected by different operational conditions. DA is suitable for solving this problem as it has been successfully used to solve the similar problem of other structural components such as bearings and gears. The structural characteristics are more complicated in maglev rail joints, which makes it necessary to extract discriminative features between damaged and normal conditions and build a DA model for maglev rail joint damage detection. Hence, as a type of novel deep TL architecture, UDDAN is proposed in this study to automatically detect different categories of maglev rail joints and mitigate the domain shift issue caused by operation mode changes.
2) In addition, this study considers the domain proximity and data distribution assumptions in the transfer loss to seek the best design for transfer loss as the model performance is highly sensitive to the collected data. The discrepancy-based DA is usually achieved through the minimization of transfer loss by measuring the discrepancy between the sample moments in the source and target domains. Meanwhile, the change in data distribution can degrade the model performance. Hence, sample moments of the first, second, and third orders and the effects of marginal and joint distributions on the discrepancy alignment in the proposed UDDAN are discussed to establish a more suitable model for maglev rail joint damage detection.

The rest of this article is organized as follows. Section II presents an overview of DA and describes the discrepancy-based DA framework and different types of data distribution. Section III introduces the UDDAN architecture. Section IV describes the experiment conducted on maglev rail joints to obtain the dataset. Section V describes the different methods with different discrepancies and data distributions for the UDDAN and discusses the results. Section VI presents the conclusion.

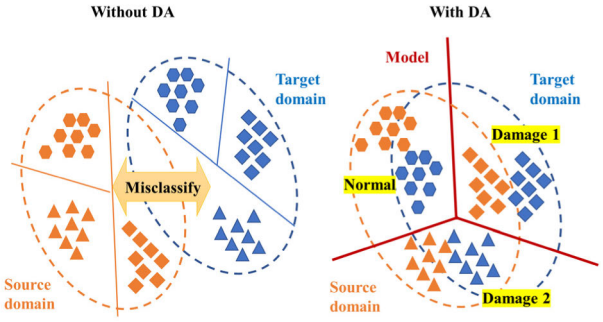

Fig. 1. Mechanism of DA for addressing domain shift.

II. Preliminaries

A. Domain Adaptation

In machine learning methods, the domain ($\mathcal{D}$) is a set of feature spaces X with marginal distributions $P(X)$. Samples in the feature space satisfy $X = \{x_1, x_2, \ldots, x_n\} \in \mathcal{X}$. Each domain has one task ($\mathcal{T}$) aimed at learning the conditional distribution $P(Y|X)$ (also known as the predictive function). $\mathcal{Y}$ is a label space in which the samples satisfy $Y = \{y_1, y_2, \ldots, y_n\} \in \mathcal{Y}$. Two domains are considered in machine learning: the source domain ($\mathcal{D}^s = \{\mathcal{X}^s, P(X^s)\}$) with task ($\mathcal{T}^s$) and the target domain ($\mathcal{D}^t = \{\mathcal{X}^t, P(X^t)\}$) with task ($\mathcal{T}^t$). Conventional machine learning methods learn the same task ($\mathcal{T}^s = \mathcal{T}^t$) over identical domains ($\mathcal{D}^s = \mathcal{D}^t$) using labeled data x_i, y_i. Therefore, the performance of conventional machine learning methods deteriorates when task variation ($\mathcal{T}^s \neq \mathcal{T}^t$) and/or domain shift ($\mathcal{D}^s \neq \mathcal{D}^t$) occurs. This problem can be solved by applying DA and using the knowledge in $\mathcal{D}^s$ and $\mathcal{D}^t$ [30].

DA assumes that the task in the source domain is the same as that in the target domain ($\mathcal{T}^s = \mathcal{T}^t$), but the two domains are different ($\mathcal{D}^s \neq \mathcal{D}^t$). DA can be divided into two types depending on the domain divergence [21]: homogeneous DA has an identical feature space ($\mathcal{X}^s = \mathcal{X}^t$) but different data distributions ($P(X^s) \neq P(X^t)$), and heterogeneous DA has nonequivalent feature spaces ($\mathcal{X}^s \neq \mathcal{X}^t$). In addition, DA can be categorized as supervised, semisupervised, or unsupervised DA based on whether the data in task $\mathcal{T}^t$ are fully labeled, partially labeled, or unlabeled, respectively. Fig. 1 shows how DA addresses domain shift. The feature space consists of the data marked as points with various shapes according to different categories. If the model is trained using the data in the source domain, misclassification may occur in the target domain. To resolve the problem, DA aims to map the features from the source and target domains to a shared feature space and build a model with a low generalization error in the target domain.

B. Discrepancy Alignment of Data Distribution

To accomplish DA, the domain-invariant feature representations must be learned to improve the task performance. Discrepancy-based DA can learn feature representations by minimizing the discrepancy between data distributions in the source and target domains. Generally, in a neural network

considering DA, the discrepancy between data distributions is equivalent to transfer loss [31]. The discrepancy can be measured through the maximal mean discrepancy (MMD) [32] or correlation alignment (CORAL) [33].

To determine the discrepancy of data distributions in the source and target domains, the MMD maps the data in the two domains into a reproducing kernel Hilbert space (RKHS). According to the Reisz representation theorem and unit ball property of RKHS, the unbiased empirical estimate of the MMD is

$$\mathrm{MMD}\left(\mathcal{D}^s, \mathcal{D}^t\right) = \| \frac{1}{N^s} \sum_{i=1}^{N^s} \phi\left(x_i^s\right) - \frac{1}{N^t} \sum_{i=1}^{N^t} \phi\left(x_i^t\right) \|_F^2 \quad (1)$$

where x_i^s and x_i^t represent the ith samples in the source and target domains, respectively; N^s and N^t are the number of samples in the source and target domains, respectively; ϕ is the kernel function for mapping data into the Hilbert space; and $\|.\|_F^2$ is the second Frobenius norm, which represents the Euclidean distance between two distributions.

Unlike the MMD, which aligns the discrepancy only with sample means, CORAL can exploit rich statistical information and align the discrepancy with the sample mean and covariance values. The covariance can be used to measure the joint variability of samples. Assume that there exist N samples in observation $X = (X_1, X_2, \ldots, X_N)^{\mathcal{T}}$, and each sample is represented as a K-dimensional vector $X_N = \{x_1, x_2, \ldots, x_K\}$. The sample covariance between the jth and kth variables is

$$\mathrm{cov}_{j,k} = \frac{1}{N-1} \sum_{i=1}^{N} \left(x_{i,j} - \overline{x_j}\right)\left(x_{i,k} - \overline{x_k}\right) \quad (2)$$

where $\overline{x_j}$ and $\overline{x_k}$ are the sample means of the jth and kth variables, respectively.

Note that $\mathrm{cov}_{j,k}$ is equal to the sample variance when $j = k$. COV is the sample covariance matrix sized $K \times K$

$$\mathrm{COV} = \begin{pmatrix} \mathrm{cov}_{1,1} & \mathrm{cov}_{1,2} & \cdots & \mathrm{cov}_{1,K} \\ \mathrm{cov}_{2,1} & \mathrm{cov}_{2,2} & & \mathrm{cov}_{2,K} \\ \vdots & & \ddots & \vdots \\ \mathrm{cov}_{K,1} & \mathrm{cov}_{K,2} & \cdots & \mathrm{cov}_{K,K} \end{pmatrix}. \quad (3)$$

Hence, the transfer loss of CORAL is defined by two covariance matrices derived from samples in the source and target domains [33]

$$\mathrm{CORAL}\left(\mathcal{D}^s, \mathcal{D}^t\right) = \frac{1}{4K^2} \|\mathrm{COV}^s - \mathrm{COV}^t\|_F^2 \quad (4)$$

where COV^s and COV^t are the covariance matrices of samples in the source and target domains, respectively.

The sample mean and covariance values are two types of sample moments for identifying the data distribution.

Specifically, the sample mean and covariance values reflect the first- and second-order sample moments, respectively. Notably, the distribution of real-world data may be too complicated to be completely described using the first- or second-order sample moments [34]. In such cases, high-order statistics (HOS), i.e., the third-order or higher order sample moments that contain more discriminative information, can be used to estimate the data distribution [35]. Chen et al. [36] presented a universal representation of HOS as

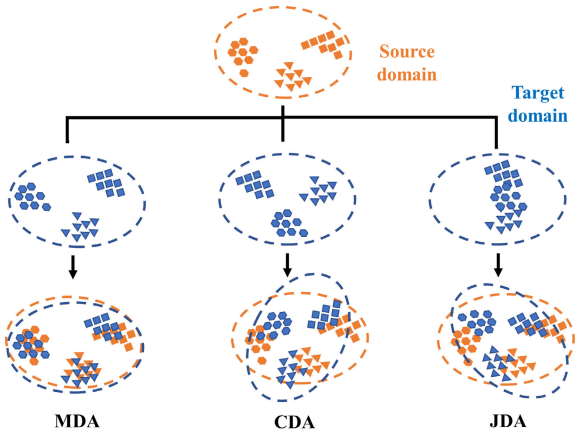

Fig. 2. Discrepancy results associated with MDA, CDA, and JDA.

$$\mathrm{HOS}\left(\mathcal{D}^s, \mathcal{D}^t\right) = \frac{1}{L^p} \| \frac{1}{N^s} \sum_{i=1}^{N^s} \theta\left(x_i^s\right)^{\otimes p} - \frac{1}{N^t} \sum_{i=1}^{N^t} \theta\left(x_i^t\right)^{\otimes p} \|_F^2 \quad (5)$$

where $\theta(x_i) = \{\theta(x_{i,1}), \theta(x_{i,2}), \ldots, \theta(x_{i,L})\}$ represents one L-dimensional feature from the ith sample, the superscript $\otimes p$ denotes the pth power tensor product, and $(1/N)\sum_{i=1}^{N} u_i^{\otimes p}$ is the pth order moment calculated by N samples.

The MMD and CORAL can be considered as special cases of the HOS formulation with $p = 1$ and $p = 2$, respectively. By setting $p = 3$ in the HOS formula, Cheng et al. [37] proposed the tricovariance (TriCOV) measure to align the discrepancy between third-order sample moments. Notably, with increasing power in the sample moment, the computing complexity increases exponentially, leading to inaccuracies in the estimated data distribution unless the sample scale is large [38]. Therefore, in this study, only cases with $p \leq 3$ are considered due to the limited computing resources and small scale of the samples.

C. Data Distribution in DA

In most DA methods, discrepancy alignment is based on the marginal distribution between the source and target domains, and the conditional distribution is assumed to be constant. However, discrepancies may occur in the conditional distribution and in the joint distribution, which is a combination of the marginal and conditional distributions. As shown in Fig. 2, the shape of the feature space influences the performance of discrepancy alignment. Different results are expected to be obtained depending on the type of distribution used in DA. However, the type of data distribution is difficult to determine due to the inaccessibility to characterize the feature space. An appropriate data distribution must be assumed to narrow the discrepancy between the source and target domains. In this study, three types of data distribution for discrepancy alignment are considered: marginal distribution alignment (MDA), conditional distribution alignment (CDA), and joint distribution alignment (JDA).

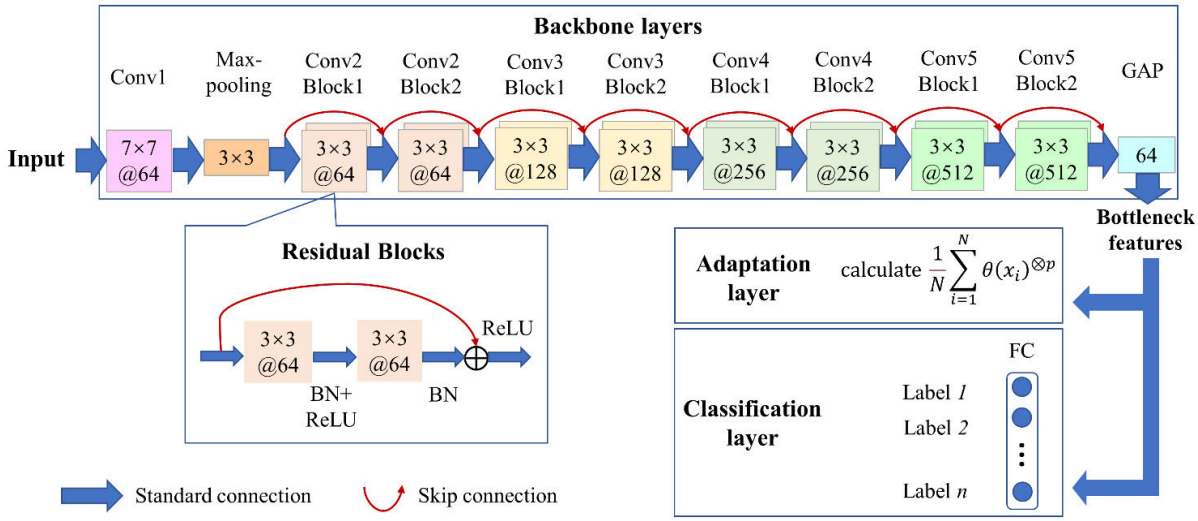

Fig. 3. Architecture of UDDAN.

MDA is aimed at narrowing the discrepancy in the data distributions in two domains ($P(X^s)$ and $P(X^t)$). The optimization objective of MDA is

$$\min d\left(P\left(X^s\right), P\left(X^t\right)\right) \tag{6}$$

where $d(\cdot)$ is an arbitrary domain discrepancy.

CDA is aimed at decreasing the discrepancy between the distributions of same-category data in two domains ($P(Y^s|X^s)$ and $P(Y^t|X^t)$). The goal of CDA can be formulated as follows [39]:

$$\min d\left(P\left(X^s|Y^s\right), P\left(X^t|Y^t\right)\right) \tag{7}$$

where $P(X^s|Y^s)$ and $P(X^t|Y^t)$ are the sufficient statistics of distributions $P(Y^s|X^s)$ and $P(Y^t|X^t)$, respectively [39]. As the target label Y^t is unknown, a pseudo label [39], obtained by testing the target data in a classifier trained using labeled source data, substitutes the target label. Based on the CDA concept, MMD can be modified to measure the discrepancy between the category-conditional distributions

$$\mathrm{CMMD}\left(\mathcal{D}^s, \mathcal{D}^t\right) = \sum_{c=1}^{C}\left\|\frac{1}{N^{s(c)}}\sum_{i=1}^{N^{s(c)}}\phi\left(x_i^s|y_i^s=c\right) - \frac{1}{N^{t(c)}}\sum_{i=1}^{N^{t(c)}}\phi\left(x_i^t|\hat{y}_i^t=c\right)\right\|_F^2 \tag{8}$$

where each category $c \in \{1, \ldots, C\}$; $N^{s(c)}$ and $N^{t(c)}$ are the number of samples with the same label category c in the source and target domains, respectively; y_i^s is the ground-truth label of the ith sample in the source domain; and $\hat{y}_i^t$ is the pseudo label of the ith sample in the target domain.

JDA integrates the advantages of MDA and CDA by simultaneously minimizing the domain discrepancy in both marginal and conditional distributions [39]. To apply the discrepancy as the transfer loss in a neural network, a deep transfer network aligning the discrepancy between joint distributions has been developed based on the MMD criterion [40]

$$\mathrm{JMMD}\left(\mathcal{D}^s, \mathcal{D}^t\right) = \xi_1\mathrm{MMD}\left(\mathcal{D}^s, \mathcal{D}^t\right) + \xi_2\mathrm{CMMD}\left(\mathcal{D}^s, \mathcal{D}^t\right) \tag{9}$$

where ξ_1 and ξ_2 are adjustable terms for the marginal and conditional distributions. This concept has been used to develop several deep transfer networks with JDA [41], [42].

III. Unsupervised Discrepancy-Based DA Network

A. Architecture of UDDAN

This article proposes the UDDAN model for maglev rail joint condition detection. As shown in Fig. 3, the UDDAN consists of several backbone layers for extracting the discriminative features of every maglev rail joint condition, an adaptation layer for learning the cross-domain invariant features, and a classification layer for evaluating the maglev rail joint conditions.

The architecture of the backbone layers is based on ResNet18 [43], consisting of five convolution layers labeled Conv1 to Conv5. Conv1 contains one convolution calculation. The other convolution layers contain two residual blocks with two convolution calculations. The skip connection is set in the residual block to avoid the decrease in accuracy as the network deepens. Batch normalization and rectified linear unit are added in each convolution calculation to promote convergence in model training. In the Conv1 layer, max-pooling layer, and first convolution calculations of Conv3, Conv4, and Conv5, the stride is set as 2 to decrease the width and height of the feature maps by half. Thus, at the end of the convolution layers, the width and height are 1/32 of the original dimension. A 7×7 filter is used in the Conv1 layer and 3×3 filters are used in the max-pooling layer and other convolution layers. The number of filters increases gradually with the deepening of the feature map. Therefore, 64, 128, 256, and 512 filters are applied in the Conv2, Conv3, Conv4, and Conv5 layers, respectively. Consequently, a 512-D feature map is condensed into a 64-D vector in global average pooling, which is named

the bottleneck feature as it is located at the bottleneck position in the model [44].

After the backbone layer calculations, the bottleneck features are exported to the classification and adaptation layers. As a fully connected (FC) layer, the classification layer nonlinearly maps the bottleneck feature to the prediction on probability for each condition of a maglev rail joint. The length of the FC layer is equal to the number of considered maglev rail joint conditions. In the classification layer, the damage classification loss ($\mathcal{L}_D$) is calculated to compare the prediction with the ground truth. The adaptation layer stores the bottleneck features from various domains to calculate the discrepancies between domains that are measured by sample moments of various orders under different data distribution assumptions. In the adaptation layer, the discrepancy value is equal to the transfer loss ($\mathcal{L}_{\mathcal{T}}$).

B. Model Training

The model is trained based on alternating forward propagation of feature generation and backpropagation of loss calculation for updating the model parameters. In this study, the loss used in model training is $\mathcal{L}_{\text{TOTAL}}$, which is a combination of the damage classification loss ($\mathcal{L}_D$) and transfer loss ($\mathcal{L}_{\mathcal{T}}$) [45]

$$\mathcal{L}_{\text{TOTAL}} = \mathcal{L}_D + \lambda L_{\mathcal{T}}. \tag{10}$$

The damage classification loss aims to match the labels between the prediction and the ground truth

$$\mathcal{L}_D = \frac{1}{N^s}\sum_{i=1}^{N^s} J\left(f\left(x_i^s\right), y_i^s\right) \tag{11}$$

$$J\left(f\left(x_i^s\right), y_i^s\right) = -\left[y_i^s \log f\left(x_i^s\right) + \left(1 - y_i^s\right)\log\left(1 - f\left(x_i^s\right)\right)\right]. \tag{12}$$

For the ith sample in the source domain, y_i^s and $f(x_i^s)$ denote the probability of each category obtained from the ground truth and prediction, respectively. $f(\cdot)$ is the predictive function learned from the backbone layers. $J(\cdot,\cdot)$ is the cross-entropy loss function that is used to match the difference between the true and predicted labels.

The transfer loss aims to realize DA from the source to the target domain. To consider different data distributions, a universal paradigm of the transfer loss is defined as

$$\mathcal{L}_{\mathcal{T}} = \xi_1 d_M\left(\mathcal{D}^s, \mathcal{D}^t\right) + \xi_2 d_C\left(\mathcal{D}^s, \mathcal{D}^t\right) \tag{13}$$

where $d_M(\cdot,\cdot)$ and $d_C(\cdot,\cdot)$ are the discrepancies between two marginal data distributions and conditional distributions, respectively, and ξ_1 and ξ_2 are the adjustable terms for the considered data distributions. If only $\xi_2 = 0$ or if only $\xi_1 = 0$, the case corresponds to MDA and CDA, respectively. The case pertains to JDA if $\xi_1 \neq 0$ and $\xi_2 \neq 0$.

In this study, the loss backpropagation is based on the stochastic gradient descent optimizer, which prevents the training procedure from falling into the saddle points in a minibatch. Backpropagation is aimed at optimizing the three model parameters (θ_b, θ_b, and θ_a) obtained from the backbone layers, classification layer, and adaptation layer, respectively

$$\theta_b \leftarrow \theta_b - \eta\frac{\partial \mathcal{L}_{\text{TOTAL}}}{\partial \theta_b} \tag{14}$$

$$\theta_c \leftarrow \theta_c - \eta\frac{\partial \mathcal{L}_D}{\partial \theta_c} \tag{15}$$

$$\theta_a \leftarrow \theta_a - \eta\frac{\partial \mathcal{L}_{\mathcal{T}}}{\partial \theta_a} \tag{16}$$

where η is the learning rate. Fig. 4 shows the training procedure. First, the model parameters, source label predictions, and bottleneck features are obtained. If JDA is applied, pseudo-target labels are required. Both the damage classification loss and the transfer loss are optimized to update the model parameters and pseudo-labels. After sufficiently optimizing the loss, a satisfactory model is obtained for directly testing the data from the target domain. Algorithm 1 summarizes the training steps.

Algorithm 1 Training Procedure of UDDAN

Input: labeled data from source domain $\{x_i^s, y_i^s\}_{i=1}^{N^s}$, unlabeled data from target domain $\{x_i^t\}_{i=1}^{N^t}$, UDDAN model architecture, and model hyperparameters

Output: the predicted label for data from the target domain

1) Train the data from the source and target domains to obtain the bottleneck features, source label predictions $\{f(x_i^s)\}_{i=1}^{N^s}$, and model parameters $\theta_b, \theta_c, \theta_a$.
2) Predict the pseudo-labels $\{\hat{y}_i^t\}_{i=1}^{N^t}$ from samples in $\{x_i^t\}_{i=1}^{N^t}$ if using JDA
3) **for** each epoch:
4) **for** each minibatch:
5) Calculate the loss functions $\mathcal{L}_D$ by (10), $\mathcal{L}_{\mathcal{T}}$ by (12) and $\mathcal{L}_{TOTAL}$ by (13)
6) Update the model parameters by solving (14)-(16)
7) Update the pseudo-labels if using JDA
8) **until** the current epoch reaches the maximum value
9) Evaluate the model performance over data from the target domain

To accelerate training, the learning rate of the model is typically set to a high value. However, the use of a high learning rate in the complete training process may lead to loss oscillation. Hence, in this study, the model learning rate is initialized with a high value and then gradually decreases as the number of training epochs increases. The learning rate η_i at the ith epoch is

$$\eta_i = \eta_0\left(1 + \frac{0.001i}{\varepsilon}\right)^{-\delta} \tag{17}$$

where ε is the number of epochs and δ is the learning rate decay.

The tradeoff term λ_i in (18) at the ith epoch is

$$\lambda_i = w\left(\frac{2}{1 + \exp\left(-\frac{10i}{\varepsilon}\right)} - 1\right) \tag{18}$$

where w is the weight term. The magnitude of $\mathcal{L}_D$ is stable but that of $\mathcal{L}_{\mathcal{T}}$ changes sharply because different sample moments are used as discrepancies. To ensure the reliability of model

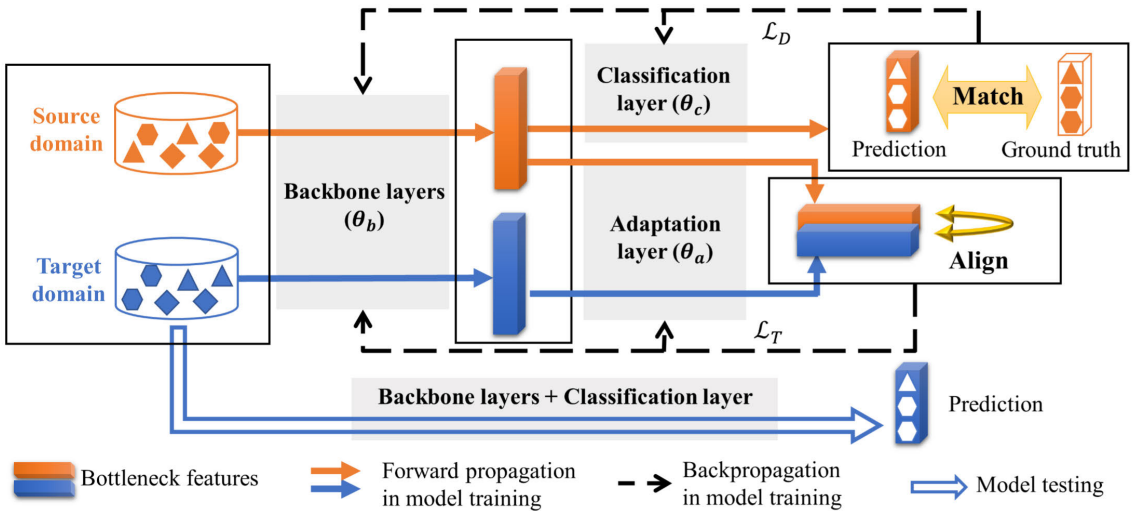

Fig. 4. Process flow of UDDAN training.

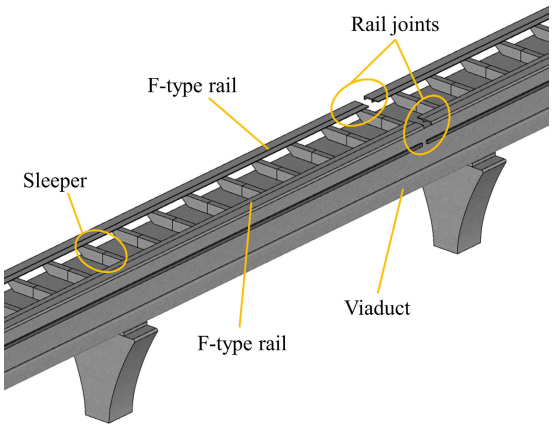

Fig. 5. Maglev guideway structure.

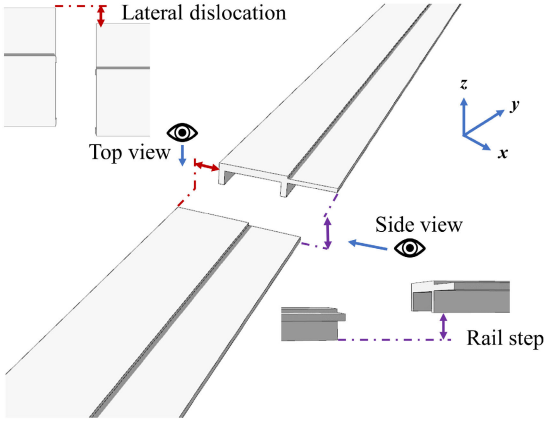

Fig. 6. Geometrical properties of a JI-type maglev rail joint.

training, the weight term is set such that the magnitudes of $\mathcal{L}_D$ and $\mathcal{L}_T$ are balanced. The remaining term guides the focus of model training in different stages, that is, emphasizes classification over the early epochs and adaptation over the later epochs [31].

To accelerate convergence and reduce the loss oscillations in model learning, the momentum term μ is used [47]. The momentum is iterated as follows:

$$\upsilon := \mu\upsilon - \eta\nabla \tag{19}$$

$$\theta := \theta + \upsilon. \tag{20}$$

IV. Experimental Study and Data Collection

A. Condition Monitoring System

As shown in Fig. 5, the maglev guideway consists of a steel sleeper, an F-type rail, and a viaduct, and the maglev rail joints are located between adjacent F-type rails. Fig. 6 shows the JI-type maglev rail joint, which is the most used type of maglev rail joint. This maglev rail joint has three main geometrical parameters: height of the rail step along the z-axis, length of the lateral dislocation along the x-axis, and width of the longitudinal gap along the y-axis. According to observations on commercial and testing maglev lines, JI-type maglev rail joints can be damaged because of bolt looseness and installation errors, which can lead to deviations in the height of the rail step or the length of the lateral dislocation, respectively. Consequently, the condition of JI-type maglev rail joints must be accurately monitored.

To verify the effectiveness of the proposed UDDAN for maglev rail joint condition detection, an experimental study is performed using the data collected from the condition monitoring system installed on the Shanghai Lin-Gang maglev test line. This line includes a straight segment, a curve segment, a slope segment, and a turnout, and the total length is 1.7 km. This study focuses on the damage detection of maglev rail joints on the straight segment. The straight segment is a multispan simply supported guideway that consists of a viaduct and several F-type rails, and the JI-type maglev rail joint is used to connect two F-type rails, as shown in Fig. 7.

A customized online monitoring system (see Fig. 8) is used to monitor the condition of maglev rail joints. This system consists of a set of piezoelectric (PZT)

Fig. 7. Maglev rail joint on the straight segment of Shanghai Lin-Gang maglev test line.

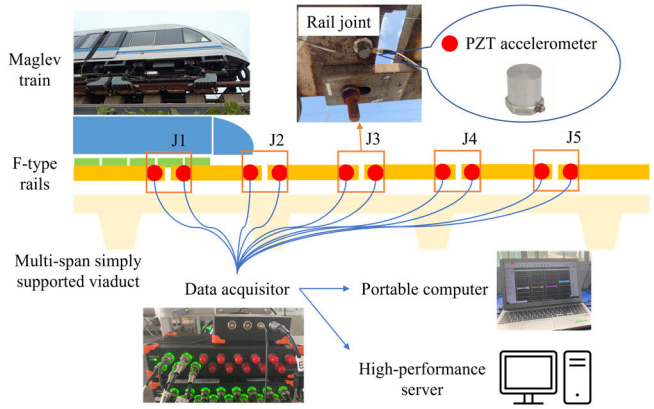

Fig. 8. Condition monitoring system for maglev rail joints.

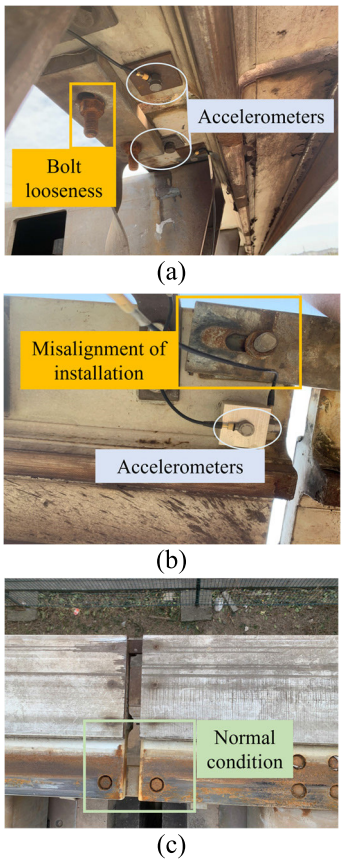

Fig. 9. Maglev rail joints with (a) rail step damage, (b) lateral dislocation damage, and (c) in normal (damage-free) condition.

accelerometers with anti-electromagnetic interference (EMI) capability, multiple-channel data acquisition unit (16)-channel DEWESOFT-SIRIUS) for data collection, portable computer for data storage, and high-performance server for data processing. Ten PZT accelerometers are applied to monitor five maglev rail joints labeled J1–J5, covering a monitoring range of approximately 80 m. For each maglev rail joint, two accelerometers are mounted on the cantilevered side of the adjacent ends of two F-type rail sections to measure the vertical accelerations. All the maglev rail joints are considered to operate in the same weather condition. To avoid the EMI generated by the maglev system, the deployed sensors, signal cables, and data acquisition unit are insulated. Data are sampled at a frequency of 5000 Hz to ensure sufficient signal acquisition resolution to capture the high-frequency components resulting from the damage. The DEWESOFT-SIRIUS instrument can be triggered automatically to acquire and store data during the maglev train passage. A high-performance server with eight cores, 16 threads, and 64-GB memory is used to facilitate the multiple damage detection at various maglev rail joints. The maglev trains run at speeds of 20–60 and 10–20 km/h in the stable passing and braking modes on the test line, respectively.

B. Dataset

Within the experimental period from December 2020 to March 2021, two types of damage are observed, as shown in Fig. 9(a) and (b): a lateral dislocation of approximately 2 mm caused by the installation misalignment at J2, and a large rail step caused by the bolt looseness at J1 and J4. Joints J3 and J5 operate in damage-free conditions, as shown in Fig. 9(c). In other words, the data recorded from this experimental period cover three states of maglev rail joints. The maglev train with a length of 16 m runs on the rail line with two operation modes. To adequately record the rail response for each trial run, the data acquisition unit collects the recording every 10 s, and each recording is treated as one sample to be used in the training or testing of the UDDAN.

The extracted samples are preprocessed through signal analysis in both the time and frequency domains by using the time series and power spectral density (PSD), respectively. Figs. 10 and 11 show the results of time- and frequency-domain analyses for three maglev rail joint conditions in the two operation modes, respectively. Fig. 10 shows that, in both modes, the peak acceleration in the rail step is at least double that in the lateral dislocation and even 20 times that in the normal condition (no more than 10 m/s^2). Fig. 11 shows that the damaged maglev rail joints have higher PSD values in the two modes than the normal maglev rail joint. Overall, the vibration magnitude in the case of damage is larger than that in the normal condition. Moreover, the vibration is more severe in the case of rail step damage than in lateral dislocation. However, the maglev rail joint conditions cannot always be evaluated using the vibration magnitude from only the time- or frequency-domain analysis. Specifically, although the joint conditions may be clearly detected in the stable passing mode, it might be difficult to detect damage in the braking mode, due to the

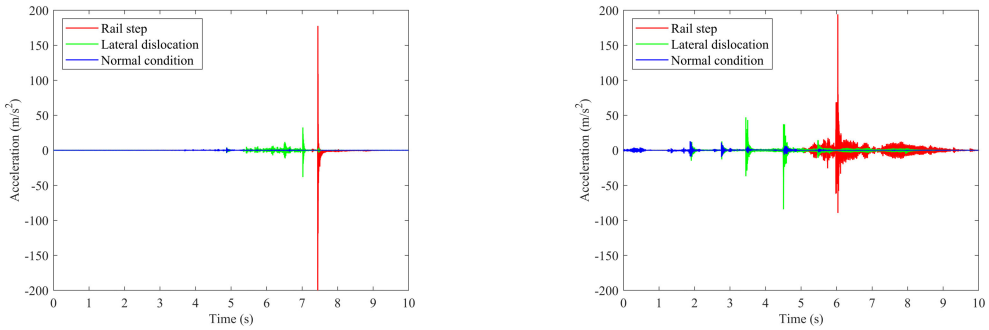

Fig. 10. Time series for (a) stable passing and (b) braking mode.

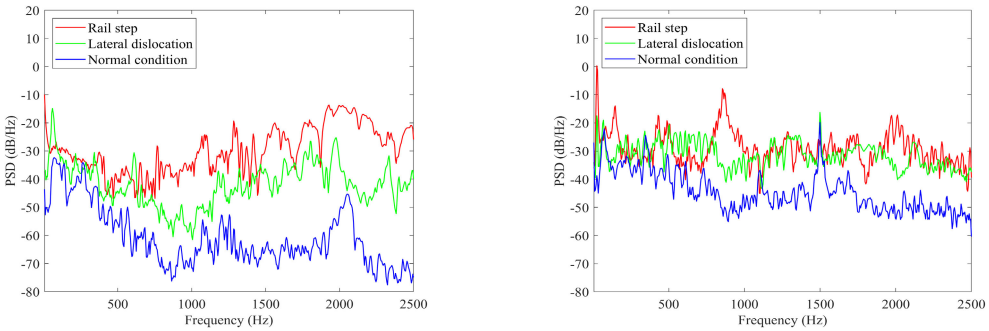

Fig. 11. PSDs for (a) stable passing and (b) braking mode.

small difference in the PSD values between the normal and damage conditions, as shown in Fig. 11(b). In addition, the varying running speeds and train weights may affect the peak accelerations and vibration frequencies at a maglev rail joint. Hence, the instantaneous features of a maglev rail joint must be simultaneously extracted in the time and frequency domains. As the TFSs consist of feature information in both time and frequency domains, TFSs are derived in this study to effectively extract the time–frequency features from the collected data [46]. Wang et al. [18] highlighted that the discriminative features among the three conditions of maglev rail joints can be explicitly derived using the TFSs. Fig. 12 shows the TFSs obtained from the data associated with the maglev rail joints in the three conditions and two modes. The discriminative features in the three conditions shift when the train moves from the stable passing mode to the braking mode. Moreover, the discriminative features in the braking mode are not as explicit as those in the stable passing mode. For example, TFSs for the normal condition [see Fig. 12(d)] and lateral dislocation [see Fig. 12(e)] are similar, and the classifier may not be able to easily extract and distinguish the discriminative features between these conditions. In other words, a classifier trained over the stable passing (breaking) mode may fail when applying to data from the braking (stable passing) mode.

Assuming that each domain represents an operation mode, the UDDAN can be used to extract the seemingly similar discriminative features between the two modes. The considered problem is a typical homogeneous DA problem, given that: 1) the source and target tasks are the same, i.e., to identify the three conditions of maglev rail joints; 2) the feature space in the source and target domains is the same, i.e., both domain contain the TFSs extracted by maglev rail joints; and 3) the data, or samples, are distributed inconsistently in the source and target domains, i.e., the TFSs are collected from different operation modes.

TABLE I
NUMBERS OF TFS SAMPLES FOR TASK A ($S_1 \rightarrow B_1$)

Domain	Normal condition	Lateral dislocation	Rail step
Source domain (stable passing)	3654	3756	3888
Target domain (braking)	1206	1392	1212

TABLE II
NUMBERS OF TFS SAMPLES FOR TASK B ($B_1 \rightarrow S_1$)

Domain	Normal condition	Lateral dislocation	Rail step
Source domain (braking)	1206	1392	1212
Target domain (stable passing)	3654	3756	3888

Tables I–III present the scale of samples (TFSs) input to the UDDAN. The two datasets consisting of the data collected from the stable passing mode are labeled S_1 and S_2. One dataset consisting of the data collected from the braking mode is labeled B_1. Three tasks are designed: task A, $S_1 \rightarrow B_1$; task

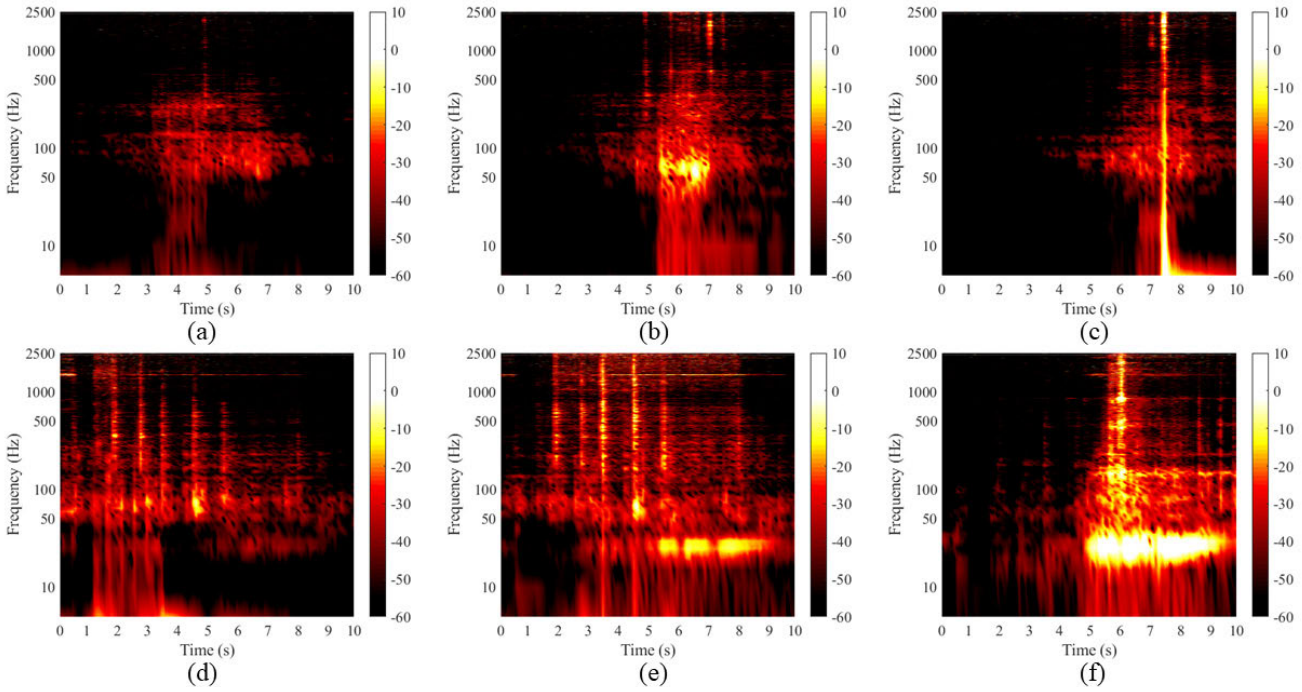

Fig. 12. TFSs for (a)–(c) stable passing and (d)–(f) braking mode. (a) and (d) In normal condition, (b) and (e) with lateral dislocation damage, and (c) and (f) with rail step damage.

TABLE III
NUMBERS OF TFS SAMPLES FOR TASK C ($S_2 \rightarrow B_1$)

Domain	Normal condition	Lateral dislocation	Rail step
Source domain (stable passing)	1470	1332	1242
Target domain (braking)	1206	1392	1212

B, $B_1 \rightarrow S_1$; and task C, $S_2 \rightarrow B_1$, where $S \rightarrow B$ denotes the transfer from stable passing to braking mode and $B \rightarrow S$ denotes the transfer from braking to stable passing mode. The designed tasks cover two potential scenarios typically encountered in real applications.

Scenario 1: The feasibility of using the different operation modes as the source domain is discussed because labeled maglev rail joint data may be available for only a certain operation mode. Among the two considered operation modes, one is set as the source domain and the other is set as the target domain. Therefore, this scenario involves tasks A (stable passing to braking) and B (braking to stable passing).

Scenario 2: The feasibility of setting different numbers of samples between the source and target domains is discussed because the data scale of the maglev rail joint may differ across different operation modes. To vary the number of samples, a portion of data is randomly extracted from dataset S_1 to form dataset S_2, while dataset B_1 remains unchanged. This scenario involves the comparison of tasks A and C, which have a large and small number of samples, respectively.

C. Procedure of Maglev Rail Joint Detection

To demonstrate the process of the proposed UDDAN for maglev rail joint detection, a flowchart depicting the procedure of maglev rail joint detection is represented in Fig. 13. First, the condition monitoring system (described in Section IV-A) is installed to record the acceleration data at the location of maglev rail joints when the maglev train operates under the stable passing mode and braking mode. Then, the collected data are transmitted to the portable computer and divided into different segments according to the given operation mode. The flowchart takes an example when the stable passing mode is the source domain and the braking mode is the target domain. Using the raw acceleration data, the TFSs from both the source and target domain are generated (as shown in Section IV-B). The dataset of TFSs is used to establish a UDDAN model. The model performance is evaluated by inputting target data to compare the prediction labels and true labels. Finally, the well-trained model is saved and employed for the classification of three categories of maglev rail joints.

V. RESULTS AND DISCUSSION

A. Comparison Methods

To illustrate the superiority of using discrepancy-based DA and evaluate the combination of different data distribution assumptions and domain discrepancies on the model performance of maglev rail joint damage detection, the following seven methods are used for comparison. In the domain-adaptation-free (DAF) method, no information across domains is provided, and thus, the model is trained only from the source domain and then tested directly over the data from the target domain. In contrast, the other six methods adopt DA and obtain the cross-domain information by calculating the domain discrepancies as the transfer loss. The two data distribution assumptions are MDA and JDA. The source and target domains are aligned by three types of discrepancies

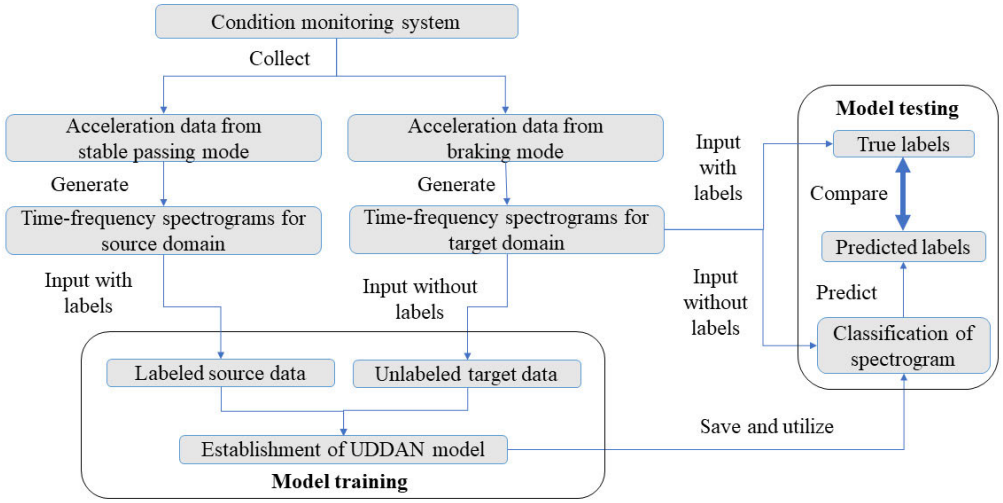

Fig. 13. Flowchart for the procedure of maglev rail joint detection.

TABLE IV
UDDAN HYPERPARAMETERS

Hyperparameter	Value
Adjustable term of transfer loss (ξ_1, ξ_2)	$\xi_1 = 1, \xi_2 = 0$ (MDA) $\xi_1 = 1, \xi_2 = 1$ (JDA)
Weight term of transfer loss (w)	1 (MMD), 10^2 (CORAL), 10^4 (TriCOV)
Initial learning rate (η_0)	0.001
Learning rate decay (δ)	0.75
Momentum (μ)	0.9
Input size of TFS sample	224×224
Mini-batch size per iteration	8
Iterations per epoch	100
Epoch (ε)	50

(MMD, CORAL, and TriCOV), with each discrepancy evaluated considering MDA and JDA.

1) *DAF:* The DAF framework that neglects the transfer loss in the UDDAN.
2) *M-MMD:* MDA based on the discrepancy of sample means.
3) *M-CORAL:* MDA based on the discrepancy of sample covariances.
4) *M-TriCOV:* MDA based on the discrepancy of sample third-order moments.
5) *J-MMD:* JDA based on the discrepancy of sample means.
6) *J-CORAL:* JDA based on the discrepancy of sample covariances.
7) *J-TriCOV:* JDA based on the discrepancy of sample third-order moments.

To fairly compare these methods, the UDDAN hyperparameters are set, as listed in Table IV. To augment the dataset, TFS samples are randomly cropped as the model input with an image resolution of 224 × 224 that fits the default width/height ratio configuration of the ResNet backbone. The training procedure involves 50 epochs, corresponding to 5000 iterations. The mini-batch size is 8, which indicates that the total training loss among eight samples in both the source and target domains is calculated per iteration. The model is developed on a server with a two-processor Intel Xeon Gold 5217 CPU and an Nvidia Tesla P40 GPU. The programming language is Python 3.7, and the programming environment is based on PyTorch 1.8.1 and the Windows Server 2016 Platform.

B. Quantitative Evaluation of Model Performance: Classification Accuracy, Domain Proximity, and Transfer Loss

As the most important criterion in evaluating the model performance, the classification accuracy associated with the classification layer is determined as the percentage of the number of correctly predicted samples over the total samples in the target domain

$$\text{Acc} = \frac{1}{N^t} \sum_{i=1}^{N^t} \text{sign}\left(f\left(x_i^t\right) = y_i^t\right) \tag{21}$$

where sign(·) is the indicator function, which is equal to 1 and 0 if the condition is true and false, respectively; and $f(x_i^t)$ and y_i^t are the predicted and true labels for the ith sample in the target domain, respectively. The classification results are obtained using the model corresponding to the epoch with the smallest training loss.

To verify the performance of DA method, the domain discrepancy in the adaptation layer is quantified. Ben-David et al. [48] proposed the proxy-A-distance (PAD) to measure the similarity between the feature representations of samples from the source and target domains in DA problems. The samples obtained from the bottleneck features are used to calculate the PAD, as these features are typically used for discrepancy alignment in the adaptation layer. The PAD is calculated as

$$\text{PAD} = 2(1 - 2\epsilon) \tag{22}$$

TABLE V
CLASSIFICATION ACCURACY (%) OF DIFFERENT METHODS

Task	DAF	M-MMD	J-MMD	M-CORAL	J-CORAL	M-TriCOV	J-TriCOV
A	86.75	86.56	94.41	94.38	94.46	91.84	92.34
B	83.97	83.97	94.80	94.91	94.59	88.99	89.74
C	83.44	83.52	89.76	88.85	89.24	88.22	88.03

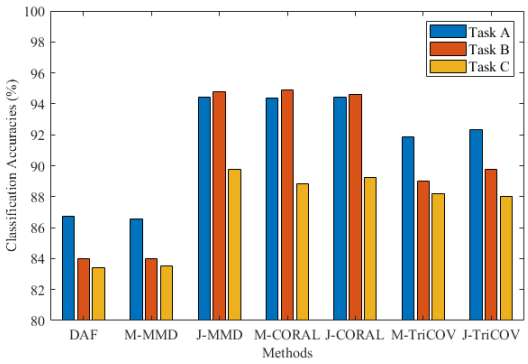

Fig. 14. Classification accuracy (%) of different methods.

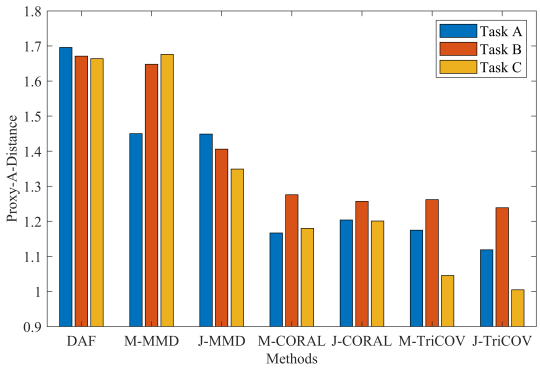

Fig. 15. PAD between bottleneck features from different methods.

where ϵ is the generalization error of the classifier tested on the merged samples from the source and target domains. A smaller PAD corresponds to a larger generalization error, which is attributable to less distinguished samples from the source and target domains. Hence, a smaller PAD indicates more similar feature representations between the source and target domains, that is, higher domain proximity. The PAD is calculated using a binary classifier that is based on a linear support vector machine.

Table V and Fig. 14 present the classification accuracies for the three conditions of the maglev rail joint. The classification accuracies of the seven methods for the three tasks are all higher than 83%, which shows that the proposed model can effectively classify the different conditions of maglev rail joints. Moreover, the accuracies of the six methods based on DA are higher than those of the DAF model, which shows that the incorporation of DA enhances the model performance.

Notably, the accuracies of M-MMD in the three tasks are similar to those of DAF, which indicates that MMD in MDA does not significantly enhance the model performance. However, the accuracies of J-MMD are considerably higher than those of the DAF. These results show that the conditional distribution must be considered when using MMD as the discrepancy.

The accuracies of M-CORAL and J-CORAL are the highest among the six methods (higher than 94% for tasks A and B and approximately 90% for task C), which indicates that the consideration of CORAL in MDA and JDA can increase the classification accuracy. The accuracies of M-TriCOV and J-TriCOV for the three tasks are smaller than those of M-CORAL and J-CORAL. In other words, the use of TriCOV may decrease the accuracy. These results demonstrate that sample moments with the second order may be optimal for setting the discrepancy.

Further increase in the order can degrade the model performance, potentially because the alignment of high-order sample moments involves a complicated calculation, which may lead to overfitting in model training and decrease the classification accuracies. Moreover, the accuracies are nearly identical for M-CORAL and J-CORAL, and for M-TriCOV and J-TriCOV. This similarity indicates that the consideration of conditional distribution does not affect the classification accuracy when a high-order sample moment is used.

The classification accuracies of DAF, M-MMD, M-TriCOV, and J-TriCOV in task A are higher than those in task B, while the classification accuracies of J-MMD, M-CORAL, and J-CORAL in task A are close to those in task B. In other words, the domain shift affects the classification accuracies, but this influence can be eliminated using appropriate DA methods. The accuracies of all seven methods for task C are lower than those in task A, which indicates that the model performance deteriorates when the scale of the samples decreases.

The PADs of the seven methods for the three tasks are presented in Table VI and Fig. 15. The PADs associated with the DA methods are smaller than that from the DAF for all three tasks, except the PAD of M-MMD for task C. This finding demonstrates that discrepancy alignment minimizes the difference between the source and target domains. In addition, the PAD decreases with the increase in the order of sample moments (MMD > CORAL > TriCOV), especially with a significant decrease observed from the first-order sample moment (MMD) to the second-order sample moment (CORAL). In other words, the consideration of higher order sample moments enables the closer alignment of the source and target domains. Therefore, for each task, the smallest PAD is obtained by the methods using the third-order sample moment (TriCOV) as the domain discrepancy.

For a given order of sample moments, the PADs for the three tasks are similar in MDA and JDA when using CORAL and TriCOV as the domain discrepancy. However, the PADs

TABLE VI
PAD BETWEEN BOTTLENECK FEATURES FROM DIFFERENT METHODS

Task	DAF	M-MMD	J-MMD	M-CORAL	J-CORAL	M-TriCOV	J-TriCOV
A	1.696	1.450	1.449	1.167	1.204	1.175	1.119
B	1.671	1.648	1.406	1.276	1.257	1.262	1.239
C	1.664	1.676	1.349	1.180	1.201	1.046	1.005

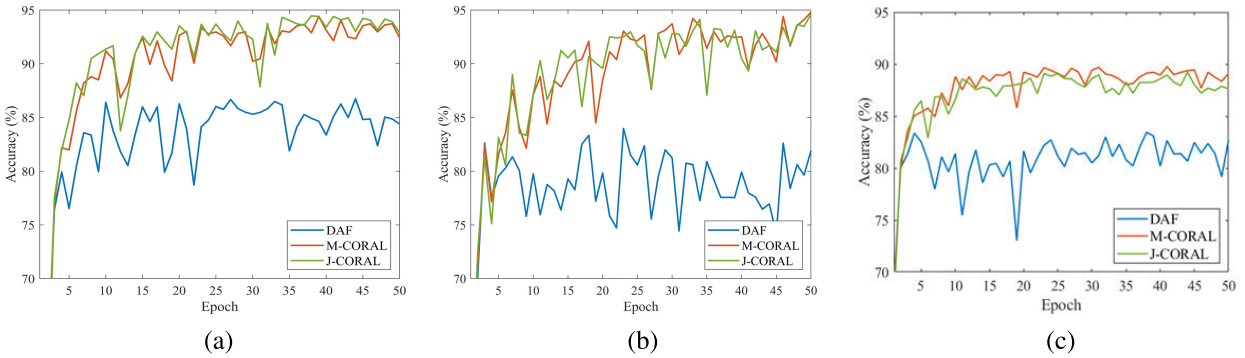

Fig. 16. Classification accuracy of DAF and two DA methods for (a) task A, (b) task B, and (c) task C with the change in the number of training epochs.

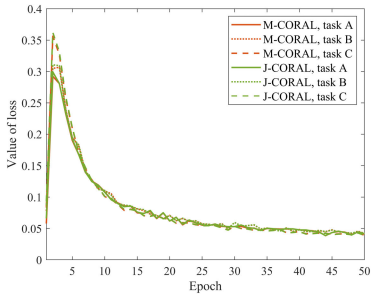

Fig. 17. Transfer loss with the training epochs for tasks A, B, and C.

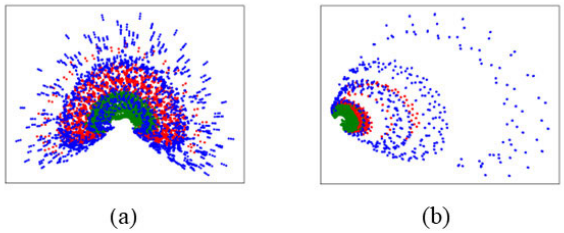

Fig. 18. Feature clustering from raw TFSs with samples extracted in (a) stable passing mode of dataset S_1 and (b) braking mode of dataset B_1.

for tasks B and C are smaller in JDA than MDA when using MMD as the domain discrepancy. In other words, the distribution assumption affects only the extent of domain proximity when using a low-order sample moment. Hence, the use of high-order sample moments can compensate for the lack of alignment between the source and target domains caused by the distribution assumption.

Overall, J-MMD, M-CORAL, and J-CORAL exhibit the highest classification accuracies, and methods considering CORAL and TriCOV can decrease the domain proximity. If MMD is used as the discrepancy, the joint distribution must be assumed to avoid the decreased domain proximity. If TriCOV is used as the discrepancy, the classification accuracies are not satisfactory. Therefore, CORAL is preferred to be used as the discrepancy in further analysis.

The convergence during model training is evaluated considering the numerical variations in the classification accuracy and transfer loss with training epochs. Fig. 16 shows the change in classification accuracy of the DAF and two recommended DA methods (M-CORAL and J-CORAL), and Fig. 17 shows the change in transfer loss.

The classification accuracy (see Fig. 16) and transfer loss (see Fig. 17) converge after training for 50 epochs. In other words, the convergence of model training can be obtained within 50 epochs. In the first five epochs, the classification accuracy in all three tasks increases to approximately 80% for the three methods, and the transfer loss for all DA methods also increases. In other words, the model training focuses on classification instead of adaptation in the first five epochs.

With training continuing to be performed, the classification accuracy does not increase significantly for task A and fluctuates for tasks B and C when the DAF is used. In comparison, the classification accuracy significantly and continuously increases when the DA methods are used. In addition, the transfer loss no longer increases after the first five epochs. In other words, the application of DA gradually enhances the model performance as the number of training epochs increases.

C. Visualization of Model Performance: Sample Clustering Based on Bottleneck Features

To intuitively observe the model performance, the TFS samples are clustered using the features contained in the samples. However, these features are too high-dimensional to be observed directly. Using a nonlinear dimensionality reduction technique, t-distributed stochastic neighbor embedding (t-SNE) [49], the high-dimensional features can be visualized in a low-dimensional space. Figs. 18–21 show the results of t-SNE-based feature visualization of TFS samples. The features are mapped into a 2-D scatter diagram. Each point in the scatter diagram represents a sample and its category is

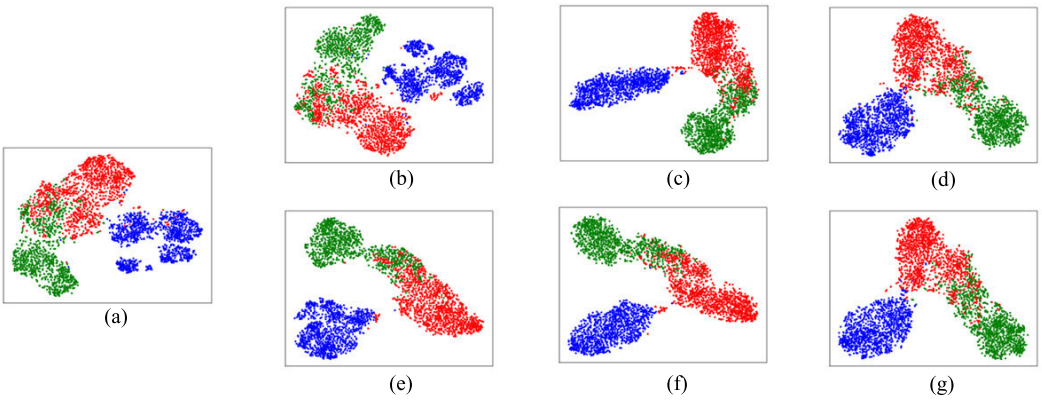

Fig. 19. Sample clustering based on bottleneck features for task A, with the samples from the braking mode. (a) DAF. (b) M-MMD. (c) M-CORAL. (d) M-TriCOV. (e) J-MMD. (f) J-CORAL. (g) J-TriCOV.

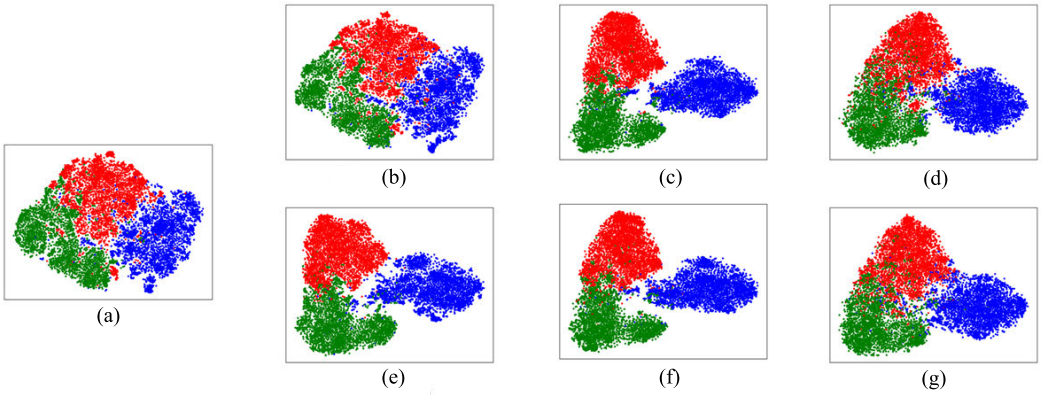

Fig. 20. Sample clustering based on bottleneck features for task B, with the samples from the stable passing mode. (a) DAF. (b) M-MMD. (c) M-CORAL. (d) M-TriCOV. (e) J-MMD. (f) J-CORAL. (g) J-TriCOV.

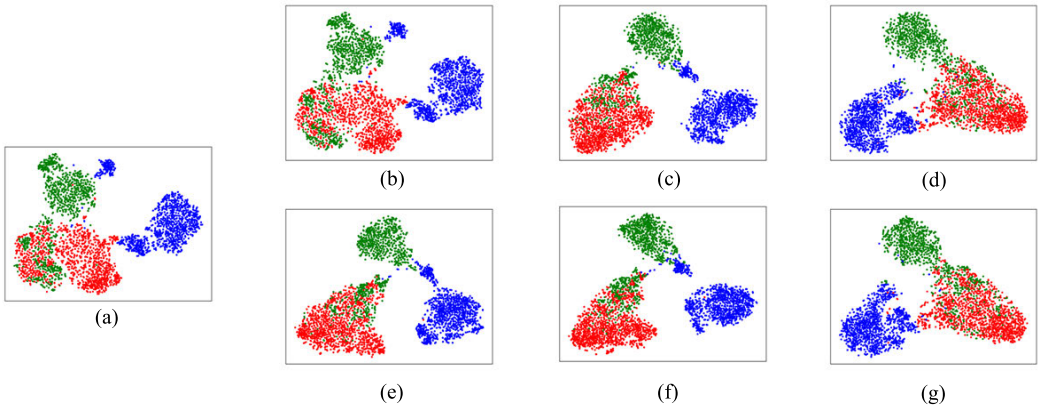

Fig. 21. Sample clustering based on bottleneck features for task C, with the samples from the braking mode. (a) DAF. (b) M-MMD. (c) M-CORAL. (d) M-TriCOV. (e) J-MMD. (f) J-CORAL. (g) J-TriCOV.

indicated by a color: green, red, and blue points correspond to samples in the normal, lateral dislocation, and rail step conditions, respectively. Fig. 18 shows the clustering results of samples of raw TFS inputs to the model. Figs. 19–21 show the sample clustering results based on bottleneck features. The bottleneck features are extracted from the target domain as the model performance is evaluated through the data from the target domain.

As shown in Fig. 18, the data distributions of the two domains have relatively clear boundaries between the three categories, and their feature space is similar but is not strictly the same. It implies the necessity of considering not only the marginal distribution but also the joint distribution. The features are distributed in a disorderly manner and cannot be clustered in either the stable passing mode [see Fig. 18(a)] or the braking mode [see Fig. 18(b)]. In contrast, as shown in Figs. 19–21, the distribution of features is relatively orderly, and the samples can be effectively classified. In other words, the discriminative features in different categories can be learned through the training of backbone layers.

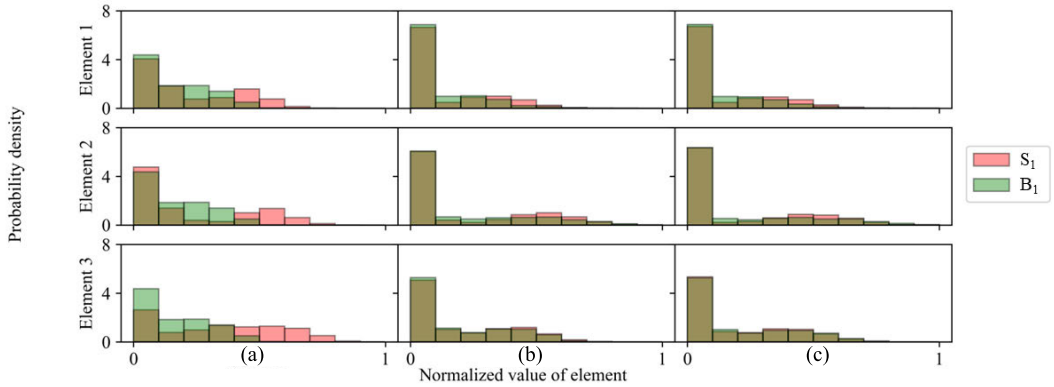

Fig. 22. Data distribution of elements from bottleneck features for task A. (a) DAF. (b) M-CORAL. (c) J-CORAL.

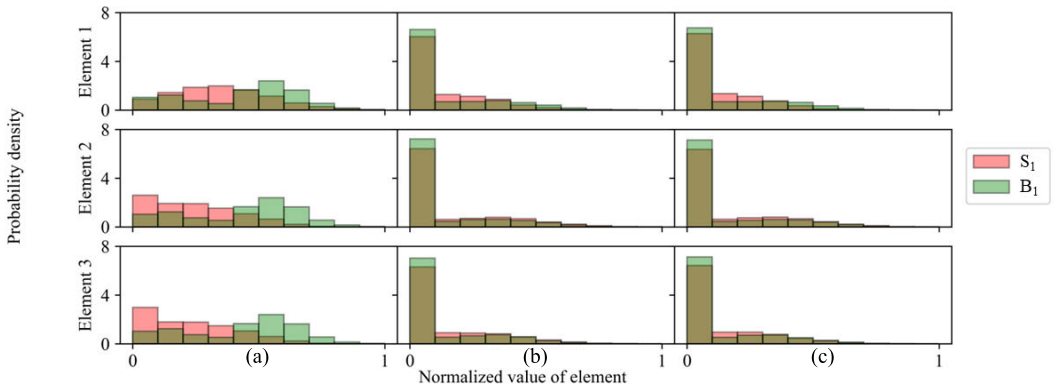

Fig. 23. Data distribution of elements from bottleneck features for task B. (a) DAF. (b) M-CORAL. (c) J-CORAL.

A better classification of samples means that the intracategory samples are more concentrated and separated. As shown in Figs. 19–21, the rail step samples are clustered tighter and are more distinguishable than the normal condition and lateral dislocation samples across the three tasks. In other words, the time–frequency features of the rail step TFSs are more likely to be recognized by the trained model to perform feature extraction. In addition, it is difficult to cluster a portion of samples for the normal and lateral dislocation conditions, which indicates a high similarity of the time–frequency features in the normal and lateral dislocation conditions and leads to decreased classification accuracies.

In task A, the clustering result of the DAF [see Fig. 19(a)] is inferior to those of nearly all DA methods [see Fig. 19(b)–(g)]. The finding highlights that the adaptation layer facilitates the sample classification, but the consideration of joint distribution hardly influences the clustering results. The only exception is M-MMD [see Fig. 19(b)], whose clustering result is basically the same as that of the DAF.

Overall, the trends in clustering results for task A can extend to tasks B and C. The DA methods, especially those based on CORAL facilitate sample clustering and enhance the model performance in tasks B and C. Therefore, the models with CORAL methods, i.e., M-CORAL and J-CORAL, are recommended. This finding is consistent with the results of the classification accuracy and domain proximity, which is reasonable because the bottleneck features are directly used for the model classification and discrepancy alignment between the source and target domains.

D. Evidence of Discrepancy Alignment: Data Distribution Comparison Between Source and Target Domain

To demonstrate the distribution shift between the source and target domains when using DA methods, the data distributions of the bottleneck features from the source and target domains are drawn. Because the bottleneck feature in the proposed model is a vector with 64 elements, it is difficult to draw the data distribution of all elements. Therefore, three elements (1)–(3) are randomly selected as representative examples. The bottleneck features are extracted through the models trained with DAF and with two recommended DA methods, i5.e., M-CORAL and J-CORAL.

Histograms, as approximate representations of the data distribution, are derived for the bottleneck features in tasks A–C, as shown in Figs. 22–24, respectively. The x-axis shows the value of the element, and the y-axis shows the probability density. The element values are normalized for probability estimation. The x-axis ranges from 0 to 1 after normalization, and the histogram contains ten equal bins. Therefore, the width of each bin is 0.1. The area of each bin in the histogram reflects the probability of occurrence for elements in a specific interval, with the width of the interval being equivalent to the bin width.

The data distribution of the source and target domains exhibits several similarities. Except for the DAF in task B

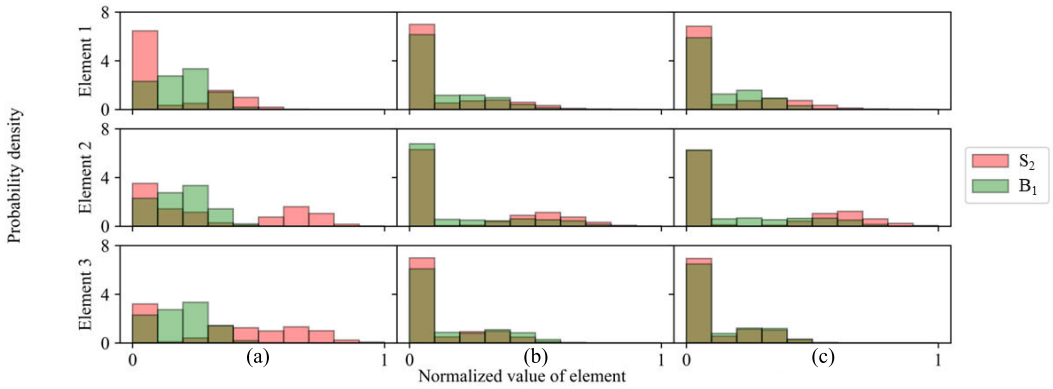

Fig. 24. Data distribution of elements from bottleneck features for task C. (a) DAF. (b) M-CORAL. (c) J-CORAL.

[see Fig. 23(a)], the data in the source and target domains exhibit positively skewed distributions. The data distributions obtained from the DAF and two DA methods are different. In general, a larger area of intersection sets in the histogram indicates higher data distribution consistency and lower discrepancy between the source and target domains. As shown in Fig. 22, the elements obtained from the DAF have the smallest area of intersection sets for the three methods in task A. In comparison, the histograms for the two DA methods are overlapped. Similar phenomena are observed in the results for tasks B (see Fig. 23) and C (see Fig. 24). These results demonstrate that DA methods can promote the discrepancy alignment of data distributions between the source and target domains.

For task A, the data distributions between the source and target domains are similar when M-CORAL [see Fig. 22(b)] and J-CORAL [see Fig. 22(c)] are used. In other words, the discrepancy between the source and target domains is similar in the cases of marginal and joint distribution assumptions. This finding also extends to tasks B (see Fig. 23) and C (see Fig. 24). Hence, the discrepancy alignment of the data distribution may not be related to the assumption of data distribution.

The necessity of selecting an appropriate sample moment can be surveyed through DAF [see Figs. 22–24(a)], which explicates the unaligned data distribution. For DAF, the distribution of the histogram is flat, and the value of elements covers a broad scope, which means that the effect of covariance cannot be ignored in the distribution alignment. Compared to MMD which only cares about the means of data, CORAL cares about both means and covariances of data, and thus, CORAL performs better than MMD. The data distributions after using CORAL show that CORAL has almost aligned the data very well, which means that the alignment with a high-order moment, e.g., TriCOV, may not bring a remarkable improvement. Overall, this verifies that CORAL is the best choice for this study.

E. Comparative Study With Other Deep DA Neural Networks

Currently, several neural networks have been developed and functioned well in solving the domain shift issue. To verify the accuracy of the proposed UDDAN, a comprehensive discussion between the UDDAN and other state-of-the-art deep neural networks is conducted. Five kinds of deep neural networks are adopted for discussion, including the deep adaptation network (DAN) [50], DeepCoral [33], the domain adversarial neural network (DANN) [29], the dynamic adversarial adaptation network (DAAN) [51], and the UDDAN. Among them, DAN, DeepCoral, and the UDDAN are discrepancy-based DA networks, while DANN and DAAN are adversarial-based DA networks. Two transfer losses of M-MMD and M-CORAL are considered in the UDDAN, but only MDA-based discrepancies are used for comparison as DAN and DeepCoral are developed only under the assumption of marginal data distribution. DAN and M-MMD use MMD as a discrepancy, and DeepCoral and M-CORAL use CORAL as a discrepancy. Only M-MMD and M-CORAL adopt the tradeoff term in the transfer loss. The classification accuracies of the five methods together with the UDDAN methods considering the two transfer losses of M-MMD and M-CORAL are shown in Fig. 25. As can be seen, M-CORAL, which is the recommended method in this study, has the highest classification accuracy for all three tasks. It is also found that the classification accuracy of M-MMD is higher than that of DAN and the classification accuracy of M-CORAL is higher than that of DeepCoral. The results indicate that the tradeoff term designed in the UDDAN contributes to the accuracy improvement. Though adversarial-based DA networks (DANN and DAAN) are superior to the first-order discrepancy-based DA networks (DAN and M-MMD), they are inferior to the

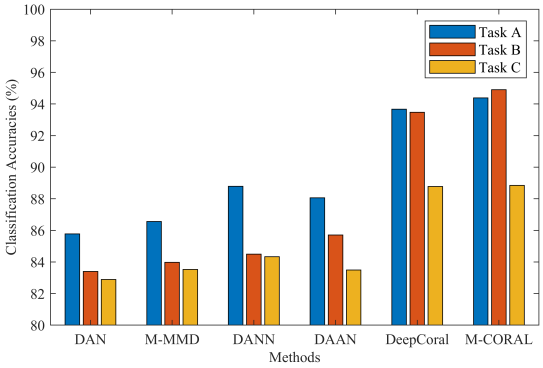

Fig. 25. Classification accuracies of UDDAN and other DL methods.

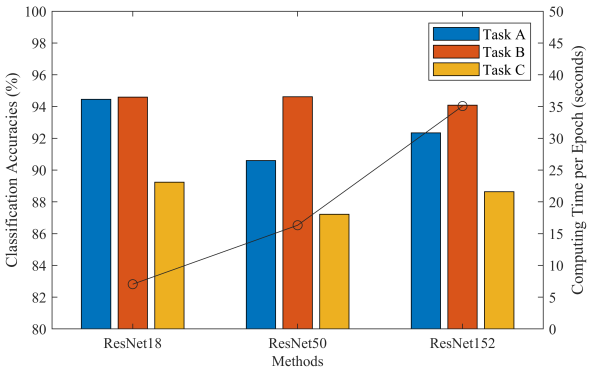

Fig. 26. Computing efficiency and classification accuracy between different ResNet backbones.

second-order discrepancy-based DA networks (DeepCoral and M-CORAL). It means that the discrepancy-based DA networks are better than adversarial-based DA networks in this study. In summary, UDDAN is more suitable than other state-of-the-art deep neural networks for the damage detection of maglev rail joints.

ResNet18 serves as the most lightweight network in a series of ResNet backbones. However, in terms of the problem considered in this article, its effectiveness is required to be further verified between different ResNet backbones. As shown in Fig. 26, a comparison is conducted between ResNet18, ResNet50, and ResNet152. A unified method of J-CORAL under the UDDAN architecture is used in training. The results show that ResNet18 spends the lowest computing time in all three networks. This is because the training time spent for ResNet18 is the least as there are the least parameters to be learned. Therefore, the model adopting ResNet18 network is easier to be converged and can be used for real-time classification. As for classification accuracy, ResNet18 is the highest after learning 50 epochs in all tasks, especially in tasks A and C. Overall, the computing efficiency and classification accuracy of the model using ResNet18 are better than the other two networks. Thus, we adopt ResNet18 as the backbone of the network in this study.

VI. Conclusion

This article proposes a discrepancy-based DA network to overcome the domain shift issue in the structural assessment of maglev rail joint conditions across various operation modes of maglev trains. An unsupervised algorithm is used to ensure the transferability of the network in real applications. Using the data from the source and target domains, the network trains the domain-invariant time–frequency discriminative features from the backbone layers and domain-variant time–frequency discriminative features from the adaptation layer. The trained model can detect the condition of maglev rail joints across different operation modes.

The applicability of the UDDAN is validated over a dataset acquired from an in situ maglev monitoring system. The results demonstrate the potential of using discrepancy-based DA in maglev rail joint damage detection. The DA is associated with the higher average classification accuracies, smaller domain distances, better clustering of samples, and more consistent data distributions of bottleneck features than the DAF. Among the six DA methods, the second-order sample moment (CORAL) is found to represent the best discrepancy for the distribution alignment, regardless of whether the marginal or joint distribution is used. In addition, the model performance is verified in three tasks. The findings highlight that the proposed discrepancy-based DA network is robust against the operational conditions in the cross-domain maglev rail joint condition assessment.

The future study includes two aspects. First, there are three types (named J-I, J-II, and J-III) of maglev rail joints in a maglev line, and each type of maglev rail joints can be regarded as a domain. In this study, only the J-I type maglev rail joint is selected as research object. The model learned from the J-I type maglev rail joint may fail to predict the J-II and J-III type maglev rail joints due to the domain shift. To extend the feasibility of the established model, the model can be verified by using data from the J-II and J-III type maglev rail joint. Second, more domain shift scenarios in maglev transport operations will be considered. For example, the vehicle loadings are not always constant. Different weights of the vehicle may cause different acceleration responses of maglev rail joints. As a result, the TFS demonstrates different discriminative features, and the effectiveness of the established model with the influence of vehicle loading needs to be further studied.

References

[1] R. M. Goodall, "Generalised design models for EMS maglev," Presented at the 20th Int. Conf. Magn. Levitated Syst. Linear Drives, San Diego, CA, USA, Dec. 2008.

[2] Y. Li, P. Yu, D. Zhou, and J. Li, "Magnetic flux feedback strategy to suppress the gap fluctuation of low speed maglev train caused by track steps," Presented at the 37th Chin. Control Conf. (CCC), Wuhan, China, Jul. 2018.

[3] H. Dangre, "A review on insulated rail joints (IRJ) failure analysis," *Int. J. Adv. Res. Publications*, vol. 3, no. 1, pp. 5–9, 2019.

[4] X. Li, M. Zhai, X. Li, and W. Dong, "Research on suppression strategy for track dislocation interference in medium-low speed maglev train," Presented at the IEEE 4th Inf. Technol., Netw., Electron. Autom. Control Conf. (ITNEC), Chongqing, China, Jun. 2020.

[5] T. E. Alberts, A. M. Hanasoge, and A. M. Omran, "On the influence of structural flexibility on feedback control stability for magnetically suspended vehicles," *J. Dyn. Syst., Meas., Control*, vol. 133, no. 5, Sep. 2011, Art. no. 051010.

[6] E. Kabo, J. C. O. Nielsen, and A. Ekberg, "Prediction of dynamic train–track interaction and subsequent material deterioration in the presence of insulated rail joints," *Vehicle Syst. Dyn.*, vol. 44, pp. 719–729, Apr. 2007.

[7] D. Zhou, P. Yu, L. Wang, and J. Li, "An adaptive vibration control method to suppress the vibration of the maglev train caused by track irregularities," *J. Sound Vib.*, vol. 408, pp. 331–350, Nov. 2017.

[8] M. Oregui, S. Li, A. Núñez, Z. Li, R. Carroll, and R. Dollevoet, "Monitoring bolt tightness of rail joints using axle box acceleration measurements," *Struct. Control Health Monit.*, vol. 24, no. 2, Feb. 2017, Art. no. e1848.

[9] M. Molodova, M. Oregui, A. Núñez, Z. Li, and R. Dollevoet, "Health condition monitoring of insulated joints based on axle box acceleration measurements," *Eng. Struct.*, vol. 123, pp. 225–235, Sep. 2016.

[10] C. Chang, L. Ling, S. Chen, W. Zhai, K. Wang, and G. Wang, "Dynamic performance evaluation of an inspection wagon for urban railway tracks," *Measurement*, vol. 170, Jan. 2021, Art. no. 108704.

[11] W. Liu et al., "An automatic loose defect detection method for catenary bracing wire components using deep convolutional neural networks and image processing," *IEEE Trans. Instrum. Meas.*, vol. 70, pp. 1–14, 2021.

[12] W. Liu, Z. Liu, H. Wang, and Z. Han, "An automated defect detection approach for catenary rod-insulator textured surfaces using unsupervised learning," *IEEE Trans. Instrum. Meas.*, vol. 69, no. 10, pp. 8411–8423, Oct. 2020.

[13] O. Avci, O. Abdeljaber, S. Kiranyaz, M. Hussein, M. Gabbouj, and D. J. Inman, "A review of vibration-based damage detection in civil structures: From traditional methods to machine learning and deep learning applications," *Mech. Syst. Signal Process.*, vol. 147, pp. 1–45, Jan. 2021.

[14] O. Abdeljaber, O. Avci, S. Kiranyaz, M. Gabbouj, and D. J. Inman, "Real-time vibration-based structural damage detection using one-dimensional convolutional neural networks," *J. Sound Vib.*, vol. 388, pp. 154–170, Feb. 2017.

[15] Y. Yu, C. Wang, X. Gu, and J. Li, "A novel deep learning-based method for damage identification of smart building structures," *Struct. Health Monit.*, vol. 18, no. 1, pp. 143–163, Jan. 2019.

[16] H. Khodabandehlou, G. Pekcan, and M. S. Fadali, "Vibration-based structural condition assessment using convolution neural networks," *Struct. Control Health Monit.*, vol. 26, no. 2, Dec. 2018, Art. no. e2308.

[17] Y. Duan, Q. Chen, H. Zhang, C. B. Yun, S. Wu, and Q. Zhu, "CNN-based damage identification method of tied-arch bridge using spatial–spectral information," *Smart Struct. Syst.*, vol. 23, no. 5, pp. 507–520, 2019.

[18] S. M. Wang et al., "Multiple damage detection of maglev rail joints using time-frequency spectrogram and convolutional neural network," *Smart Struct. Syst.*, vol. 29, no. 4, pp. 625–640, 2022.

[19] J. Quiñonero-Candela et al., *Dataset Shift in Machine Learning*. Cambridge, MA, USA: MIT Press, 2008.

[20] P. Gardner, X. Liu, and K. Worden, "On the application of domain adaptation in structural health monitoring," *Mech. Syst. Signal Process.*, vol. 138, Apr. 2020, Art. no. 106550.

[21] M. Wang and W. Deng, "Deep visual domain adaptation: A survey," *Neurocomputing*, vol. 312, pp. 135–153, Oct. 2018.

[22] A. Ozdagli and X. Koutsoukos, "Domain adaptation for structural health monitoring," Presented at the PHM Soc. Annu. Conf., Nov. 2020.

[23] X. Li, W. Zhang, Q. Ding, and J.-Q. Sun, "Multi-layer domain adaptation method for rolling bearing fault diagnosis," *Signal Process.*, vol. 157, pp. 180–197, Apr. 2019.

[24] X. Wang, H. He, and L. Li, "A hierarchical deep domain adaptation approach for fault diagnosis of power plant thermal system," *IEEE Trans. Ind. Informat.*, vol. 15, no. 9, pp. 5139–5148, Sep. 2019.

[25] X. Yu et al., "Conditional adversarial domain adaptation with discrimination embedding for locomotive fault diagnosis," *IEEE Trans. Instrum. Meas.*, vol. 70, pp. 1–12, 2021.

[26] N. Qin, B. Wu, D. Huang, and Y. Zhang, "Stepwise adaptive convolutional network for fault diagnosis of high-speed train bogie under variant running speeds," *IEEE Trans. Ind. Informat.*, vol. 18, no. 12, pp. 8389–8398, Dec. 2022.

[27] S.-X. Chen, L. Zhou, and Y.-Q. Ni, "Wheel condition assessment of high-speed trains under various operational conditions using semi-supervised adversarial domain adaptation," *Mech. Syst. Signal Process.*, vol. 170, May 2022, Art. no. 108853.

[28] J. Sresakoolchai and S. Kaewunruen, "Detection and severity evaluation of combined rail defects using deep learning," *Vibration*, vol. 4, no. 2, pp. 341–356, Apr. 2021.

[29] Y. Ganin and V. Lempitsky, "Unsupervised domain adaptation by backpropagation," Presented at the 32nd Int. Conf. Mach. Learn., Lille, France, Jul. 2015.

[30] S. J. Pan and Q. Yang, "A survey on transfer learning," *IEEE Trans. Knowl. Data Eng.*, vol. 22, no. 10, pp. 1345–1359, Oct. 2010.

[31] Y. Ganin et al., "Domain-adversarial training of neural networks," *J. Mach. Learn. Res.*, vol. 17, no. 59, pp. 1–35, 2016.

[32] K. M. Borgwardt, A. Gretton, M. J. Rasch, H.-P. Kriegel, B. Schölkopf, and A. J. Smola, "Integrating structured biological data by kernel maximum mean discrepancy," *Bioinformatics*, vol. 22, no. 14, pp. 49–57, Jul. 2006.

[33] B. Sun and K. Saenko, "Deep CORAL: Correlation alignment for deep domain adaptation," Presented at the 14th Eur. Conf. Comput. Vis., Amsterdam, The Netherlands, Oct. 2016.

[34] Y. Jia and T. Darrell, "Heavy-tailed distances for gradient based image descriptors," Presented at the 25th Conf. Neural Inf. Process. Syst., Granada, Spain, Dec. 2011.

[35] M. Gou, O. Camps, and M. Sznaier, "MoM: Mean of moments feature for person re-identification," Presented at the IEEE Int. Conf. Comput. Vis. Workshops (ICCVW), Venice, Italy, Oct. 2017.

[36] C. Chen et al., "HoMM: Higher-order moment matching for unsupervised domain adaptation," Presented at the 34th AAAI Conf. Artif. Intell., New York, NY, USA, Feb. 2020.

[37] Z. Cheng, C. Chen, Z. Chen, K. Fang, and X. Jin, "Robust and high-order correlation alignment for unsupervised domain adaptation," *Neural Comput. Appl.*, vol. 33, no. 12, pp. 6891–6903, Jun. 2021.

[38] S. J. Raudys and A. K. Jain, "Small sample size effects in statistical pattern recognition: Recommendations for practitioners," *IEEE Trans. Pattern Anal. Mach. Intell.*, vol. 13, no. 3, pp. 252–264, Mar. 1991.

[39] M. Long, J. Wang, G. Ding, J. Sun, and P. S. Yu, "Transfer feature learning with joint distribution adaptation," Presented at the IEEE Int. Conf. Comput. Vis., Sydney, NSW, Australia, Dec. 2013.

[40] X. Zhang, F. X. Yu, S.-F. Chang, and S. Wang, "Deep transfer network: Unsupervised domain adaptation," 2015, *arXiv:1503.00591*.

[41] T. Han, C. Liu, W. Yang, and D. Jiang, "Deep transfer network with joint distribution adaptation: A new intelligent fault diagnosis framework for industry application," *ISA Trans.*, vol. 97, pp. 269–281, Feb. 2020.

[42] C. Shen, X. Wang, D. Wang, Y. Li, J. Zhu, and M. Gong, "Dynamic joint distribution alignment network for bearing fault diagnosis under variable working conditions," *IEEE Trans. Instrum. Meas.*, vol. 70, pp. 1–13, 2021.

[43] K. He, X. Zhang, S. Ren, and J. Sun, "Deep residual learning for image recognition," Presented at the IEEE Conf. Comput. Vis. Pattern Recognit. (CVPR), Las Vegas, NV, USA, Jun. 2016.

[44] S.-X. Chen, L. Zhou, Y.-Q. Ni, and X.-Z. Liu, "An acoustic-homologous transfer learning approach for acoustic emission–based rail condition evaluation," *Struct. Health Monit.*, vol. 20, no. 4, pp. 2161–2181, Jul. 2021.

[45] S. Ben-David, J. Blitzer, K. Crammer, A. Kulesza, F. Pereira, and J. W. Vaughan, "A theory of learning from different domains," *Mach. Learn.*, vol. 79, nos. 1–2, pp. 151–175, May 2010.

[46] D. Verstraete, A. Ferrada, E. L. Droguett, V. Meruane, and M. Modarres, "Deep learning enabled fault diagnosis using time-frequency image analysis of rolling element bearings," *Shock Vib.*, vol. 2017, pp. 1–17, Oct. 2017.

[47] I. Sutskever et al., "On the importance of initialization and momentum in deep learning," Presented at the 30th Int. Conf. Mach. Learn., Atlanta, GA, USA, Jun. 2013.

[48] S. Ben-David et al., "Analysis of representations for domain adaptation," Presented at the 20th Conf. Neural Inf. Process. Syst., Vancouver, BC, Canada, Dec. 2006.

[49] L. van der Maaten and G. Hinton, "Visualizing data using t-SNE," *J. Mach. Learn. Res.*, vol. 9, pp. 2579–2605, Nov. 2008.

[50] M. Long et al., "Learning transferable features with deep adaptation networks," Presented at the 32nd Int. Conf. Mach. Learn., Lille, France, Jul. 2015.

[51] C. Yu, J. Wang, Y. Chen, and M. Huang, "Transfer learning with dynamic adversarial adaptation network," Presented at the 19th IEEE Int. Conf. Data Mining (ICDM), Beijing, China, Nov. 2019.

Gao-Feng Jiang received the B.S. degree in harbor waterway and coastal engineering from Zhejiang Ocean University, Zhoushan, China, in 2019, and the M.S. degree in civil engineering from the City University of Hong Kong, Hong Kong, China, in 2020. He is currently pursuing the Ph.D. degree in structural engineering with The Hong Kong Polytechnic University, Hong Kong.

His research interests include maglev structural dynamic analysis, deep learning algorithm, computer vision, and their applications in maglev damage detection.

Su-Mei Wang (Member, IEEE) received the B.S. degree in civil engineering from Hebei University, Baoding, China, in 2013, and the Ph.D. degree in bridge and tunnel engineering from Zhejiang University, Hangzhou, China, in 2018.

She is currently a Research Assistant Professor with The Hong Kong Polytechnic University, Hong Kong, China. Her research interests include structural health monitoring, high-speed railway and maglev structural dynamics, interaction of train-rail-bridge systems, vision-based deep learning, and monitoring and control in rail engineering.

Yi-Qing Ni (Member, IEEE) received the B.Eng. degree in structural engineering and the M.S. degree in structural dynamics from Zhejiang University, Hangzhou, China, in 1983 and 1986, respectively, and the Ph.D. degree in structural dynamics from The Hong Kong Polytechnic University, Hong Kong, China, in 1997.

He is currently a Yim, Mak, Kwok and Chung Professor of smart structures with The Hong Kong Polytechnic University. He is the Director of the National Engineering Research Center on Rail Transit Electrification and Automation (Hong Kong Branch), Hong Kong, and the Vice President of the International Society for Structural Health Monitoring of Intelligent Infrastructure. His research interests include structural health monitoring, structural dynamics and control, smart materials and structures, sensors and actuators, and monitoring and control in railway engineering.

Wen-Qiang Liu (Member, IEEE) received the B.S. degree in electronic information engineering and the Ph.D. degree in electrical engineering from Southwest Jiaotong University, Chengdu, China, in 2013 and 2021, respectively.

He is currently a Post-Doctoral Fellow with the National Engineering Research Center on Rail Transit Electrification and Automation (Hong Kong Branch), Hong Kong, China, and The Hong Kong Polytechnic University, Hong Kong. His research interests include artificial intelligence, computer vision, imaging, signal processing, and their applications in fault diagnosis and maintenance of high-speed railway, and maglev infrastructures.

Dr. Liu is an Associate Editor of IEEE TRANSACTIONS ON INSTRUMENTATION AND MEASUREMENT. He received the Outstanding Reviewer Award and the Outstanding Associate Editor Award from IEEE TRANSACTIONS ON INSTRUMENTATION AND MEASUREMENT in 2021 and 2022, respectively.